water

MDPI

Article

Efficient Removal of Antimony(III) in Aqueous Phase by Nano-Fe_3O_4 Modified High-Iron Red Mud: Study on Its Performance and Mechanism

Yizhe Peng [1,2], Lin Luo [1,*], Shuang Luo [1], Kejian Peng [2], Yaoyu Zhou [1], Qiming Mao [1], Jian Yang [1] and Yuan Yang [1,*]

[1] International Joint Laboratory of Hunan Agricultural Typical Pollution Restoration and Water Resources Safety Utilization, College of Resources and Environment, Hunan Agricultural University, Changsha 410128, China; pengyizhe123@sina.com (Y.P.); shuangluo@hunau.edu.cn (S.L.); zhouyy@hunau.edu.cn (Y.Z.); qimingmao@126.com (Q.M.); yangjian188@hunau.edu.cn (J.Y.)

[2] Hunan Key Laboratory of Water Pollution Control Technology, Hunan Research Academy of Environmental Sciences, Changsha 410004, China; pengkejian2003@aliyun.com

* Correspondence: luolinwei0@163.com (L.L.); yangyuan041@163.com (Y.Y.); Tel.: +86-0731-8463-8343 (L.L.)

Abstract: The resource utilization of excess red mud produced from aluminum production is a current research focus. In this study, novel nano-Fe_3O_4 modified high-iron red mud material (HRM@nFe_3O_4) was fabricated using the method of co-precipitation to remove Sb(III) from the aqueous phase. The HRM@nFe_3O_4 at a nFe_3O_4:HRM mass ratio of 1:1 had optimal adsorbing performance on Sb(III) in water. Compared with others, the synthetic HRM@nFe_3O_4 sorbent had a superior maximum Sb(III) adsorption capacity of 98.03 mg·g^{-1}, as calculated by the Langmuir model, and a higher specific surface area of 171.63 m^2·g^{-1}, measured using the Brunauer-Emmett-Teller measurement. The adsorption process was stable at an ambient pH range, and negligibly limited by temperature the coexisting anions, except for silicate and phosphate, suggesting the high selectivity toward Sb(III). HRM@nFe_3O_4 retained more than 60% of the initial adsorption efficiency after the fifth adsorption-desorption cycle. The kinetic data fitted by the pseudo-second-order model illustrated the existence of a chemical adsorption process in the adsorption of Sb(III). Further mechanism analysis results indicated that the complexation reaction played a major role in Sb(III) adsorption by HRM@nFe_3O_4. This HRM@nFe_3O_4 adsorbent provides an effective method for the removal of Sb(III) in wastewater treatment and is valuable in the reclamation of red mud.

Keywords: high-iron red mud; nano-Fe_3O_4; Sb(III); kinetics and isotherms; mechanism

Citation: Peng, Y.; Luo, L.; Luo, S.; Peng, K.; Zhou, Y.; Mao, Q.; Yang, J.; Yang, Y. Efficient Removal of Antimony(III) in Aqueous Phase by Nano-Fe_3O_4 Modified High-Iron Red Mud: Study on Its Performance and Mechanism. *Water* **2021**, *13*, 809. https://doi.org/10.3390/w13060809

Academic Editor: Domenico Cicchella

Received: 2 February 2021
Accepted: 11 March 2021
Published: 16 March 2021

1. Introduction

Antimony (Sb) is a heavy metal with high toxicity, which may result in harm to humans [1]. This element is widely found in the environment on account of rock weathering, mining and smelting activities, coal combustion, antimony product release, etc. [2]. Sb mainly exists in the forms of Sb(III) and Sb(V) in water. The species of Sb(III) are dependent on pH value: when the pH is less than 2.0, positive ionic groups play a dominant role in Sb(III), such as Sb^{3+}, SbO^+, and $Sb(OH)^{2+}$, while neutral species of $Sb(OH)_3$ and H_3SbO_3 are predominant within the pH range from 2.0 to 10.0, and when the pH of the solution is higher than 10.0, only one species of SbO^{2-} exists [3,4]. It is reported that the toxicity of Sb(III) is 10 times higher than Sb(V) [5]. Long-term ingestion of excessive Sb can cause immune system impairment, lung injury, liver damage, and even cancer [6]. Antimony and antimonic compounds have been categorized as priority pollutants by the United States Environmental Protection Agency (US EPA). The concentration of Sb in drinking water is limited to below 5 μg·L^{-1} in the European Union and 6 μg·L^{-1} by the US EPA [7,8]. Thus, effective technologies for Sb removal from aqueous solutions are of great significance to ensure the health of both the environment and human beings. Various technologies have

been applied to remove Sb from wastewater, such as coagulation or flocculation [9,10], ion-exchange [11], membrane separation [12], oxidation [13], electrochemical deposition [14], bioremediation [15] and adsorption [16]. Adsorption has attracted great attention among those technologies, with advantages such as simple operation, easy application and low cost [17].

Red mud is solid waste generated from the common process of aluminum production [18,19]. Various forms of iron and aluminum oxides are the essential ingredient of red mud, and others contain titanium dioxide, calcium carbonate, quartz, sodium aluminum silicates, etc. [20]. In 2019, the global stock of red mud was estimated to be near 4 billion tons, and the annual production amount was 0.15 billion tons [21]. According to the amount of iron, red mud can be classified into two categories: high-iron red mud, with more than 30% iron content, and low-iron red mud, with less than 30%. The high-iron red mud is more difficult to dispose of than low-iron red mud because it does greater harm to environment [22]. Due to its features of high alkalinity (pH of 10.5–12.5), complex constituents, massive generation and random disposal, it poses a great threat to ecosystems and the environment. Several leakage events caused by the random disposal of red mud have attracted much attention around the world [23,24]. Thus, the treatment of red mud is an international problem. Therefore the utilization of red mud has been explored in many fields, such as building materials, mineral extraction, catalyst and environmental remediation materials, etc. [25,26]. Red mud, with a fine porous structure and rich functional groups, has great potential to be applied as a novel absorbent to remove harmful components in wastewater [27–29]. A large amount of modified red mud was applied in the field of heavy metal pollution treatment in previous studies. For example, red-mud-modified biochar was used to adsorb As(III) and As(V) in water [30]. Functionalized material synthesized by red mud, lignin, and carbon dioxide showed good removal efficiency for the removal of Cr [31]. Fe(III)-modified, heat-treated and acid-activated red mud were utilized to remove the Mn(II) from acid wastewater [32]. However, the performance and reusability of red-mud-based materials for heavy metal removal are still unsatisfactory. Moreover, there is a lack of research reports about the removal of antimony using red mud.

Very recently, iron oxide composite adsorption materials have been regarded as promising adsorbents for heavy metal removal due to their abundant functional groups and excellent dispersibility [33,34]. In particular, Fe_3O_4 and Fe(0), which can be separated from liquid by an external magnetic field, have been widely utilized in wastewater treatment research [35,36]. At present, several innovative absorbents based on Fe_3O_4 have been investigated to remove antimony; these include Ce(III)-doped Fe_3O_4 magnetic particles [37]; Fe_3O_4 magnetic nanoparticles coated with cationic surfactants [8]; Fe_3O_4@TA@UiO-66 developed via in situ crystal growth of UiO-66 around the magnetic Fe_3O_4 modified by Tannic Acid (TA) [38]; Fe_3O_4 crosslinked by 3-aminopropyltriethoxysilane (APTES) and nitrilotriacetic acid (NTA) [39]; core-shell Fe_3O_4@Ce-Zr binary oxide [40]. Hence, nFe_3O_4 modification as a kind of mature technology could be a feasible method to improve the adsorption performance and recycling of red mud.

In this study, we aim to use the waste resources of high-iron red mud (HRM) to prepare a novel magnetic adsorbent (HRM@nFe_3O_4). This could not only remove Sb(III) from water effectively but also realize red mud reclamation and reuse. We focus on the following: (1) synthetic composition and characterization of nFe_3O_4-HRM; (2) adsorption performance of Sb(III) from aqueous solution by HRM@nFe_3O_4, including equilibrium time, maximum adsorption capacity, effects of pH, reaction temperature, initial concentration, coexisting anions and reusability; (3) the potential adsorption mechanism of Sb(III) by HRM@nFe_3O_4 via the adsorption kinetics, isotherms, functional groups analysis and binding energy analysis. This new absorbent of HRM@nFe_3O_4, with the properties of low cost and easy industrial production, could provide unique performance for Sb pollution control.

2. Materials and Methods

2.1. Materials and Reagents

The high-iron red mud was collected from the Jiaozuo alumina refinery of Aluminum Corporation of China Limited (Zhengzhou, China). The compositional matrix of the red mud used in this study is provided in Table S1. Prior to use, the red mud was dried to a constant weight in an oven at 85 °C, sieved through 100-mesh screen, and then stored in a desiccator.

Ferrous sulfate ($FeSO_4 \cdot 7H_2O$), ferric chloride ($FeCl_3$), sodium hydroxide (NaOH), hydrochloric acid (HCl), ethyl alcohol (CH_3CH_2OH), and all other analytical grade chemical reagents were bought from Sinopharm Chemical Reagent Co. Ltd. (Shanghai, China). Ultrapure water obtained by a ZOOMAC-L system (China) was used in all experiments. An Sb(III) stock solution of 1000 $mg \cdot L^{-1}$ was premade from dissolving potassium antimonyl tartrate trihydrate ($C_8H_4K_2O_{12}Sb_2 \cdot 3H_2O$) in ultrapure water. The preparation of working solutions was made in real time by diluting the stock solution with ultrapure water. An antimony standard solution containing 2% nitric acid (HNO_3) was obtained from Merck Millipore Co. Ltd. (Hong Kong, China).

2.2. Preparation of HRM@nFe$_3$O$_4$

A series of HRM@nFe_3O_4 adsorbents was synthesized at 0:1, 1:2, 1:1, 2:1 and 1:0 nFe_3O_4:HRM mass ratios using the following modified method of co-precipitation; the mass radios of 0:1 and 1:0 were pure HRM and nFe_3O_4, respectively [37,41]. First, 5.56 g $FeSO_4 \cdot 7H_2O$ and 10.80 g $FeCl_3 \cdot 6H_2O$ were dissolved in 150 mL oxygen-free water, which was prepared by filling N_2 into ultrapure water for 30–60 min. Second, under the nitrogen atmosphere, dried HRM was distributed into a 500 mL three-necked flask, which contained 200 mL oxygen-free water, and agitated for 30 min over a water bath at 60 °C. At this step, HRM@nFe_3O_4 adsorbents at nFe_3O_4:HRM mass ratios of 1:2, 1:1, 2:1 and 1:0 were obtained from different dosages of dried HRM in 9.26 g, 4.63 g, 2.32 g and 0 g, respectively. Third, in the condition of magnetic stirring and N_2 protection, the $FeSO_4 \cdot 7H_2O$ and $FeCl_3 \cdot 6H_2O$ mixed solution was added into the three-necked flask, followed by the addition of 1 $mol \cdot L^{-1}$ NaOH solution, drop-wise, until alkaline, and then aged at 60 °C for 2 h. Fourth, after cooling down to room temperature, the composites were further separated from the liquid phase by filtration, then purified by decanting and rewashing with oxygen-free water and ethanol (purged of N_2 for 30 min before use) until neutral. Finally, after vacuum drying at 95 °C for 24 h, the dried mixtures were ground into ultrafine powder and passed through a 100-mesh sieve. Additionally, nucleation and growth from the supersaturated solution was guaranteed through temperature control of the synthetic process, which could influence the size of synthesized product.

2.3. Characterization of HRM@nFe$_3$O$_4$

The surface area, pore volume and pore size of the adsorbents were measured using on Brunauer-Emmett-Teller (BET) isotherms (ASAP 2460, Micromeritics, Norcross, GA, USA). The morphology and crystallinity of HRM@nFe_3O_4 were observed using a scanning electron microscope (SEM) with energy dispersive spectrometer (EDS) (Merlin Company, ZEISS, Forchtenberg, Germany) and transmission electron microscopy (TEM) (Tecnai G2 F3, FEI, USA). The functional group(s) of nFe_3O_4-HRM were identified by Fourier transform infrared spectroscopy (FT-IR) in a spectra range from 400 to 4000 cm^{-1} wavenumber (Nicolet iS, Thermo Fisher, Waltham, MA, USA). X-ray photo-electron spectroscopy (XPS) was used to analyze the chemical states of elements on the surface of HRM@nFe_3O_4 through analysis with a spectrometer (Nexsa, Thermo Fisher, USA). The X-ray diffraction (XRD) patterns to identify the compounds contained in HRM@nFe_3O_4 were obtained from a diffractometer (Smartlab 9kW, Rigaku, Japan). The magnetic characterization of HRM@nFe_3O_4 was measured using a vibrating sample magnetometer (VSM) in the Physical Property Measurement System (PPMS) (DynaCoo, Quantum, USA). The zeta

potential of HRM@nFe$_3$O$_4$ was obtained using a zeta potential analyzer (Nano ZS90, Malvern, UK).

2.4. Batch Experiments

2.4.1. Effect of nFe$_3$O$_4$/HRM Mass Ratio

The optimized mass radio of materials (nFe$_3$O$_4$:HRM with different mass ratios of 0:1, 1:2, 1:1, 2:1 and 1:0) was acquired by comparing their adsorption capacities at 298 K with the concentration of 10 mg·L^{-1} Sb(III) solution at pH 4.6 ± 0.2. Then most efficient HRM@nFe$_3$O$_4$ was selected to apply to subsequent experiments.

2.4.2. Adsorption Isotherm and Kinetics

The adsorption isotherms of HRM@nFe$_3$O$_4$ were set at 298 K, 308 K and 318 K in the different initial Sb(III) concentrations of 5–80 mg·L^{-1}. The adsorption kinetics were conducted by sampling at the specified time under 298 K and at a pH of 4.6 ± 0.2, and the initial concentration of Sb(III) was 5, 10, and 20 mg·L^{-1}.

2.4.3. The Influence of Solution PH and Coexisting Ions

The influence of pH was adjusted to 1.6–11.6 using 1 mol·L^{-1} NaOH or HCl solution with the most efficient HRM@nFe$_3$O$_4$ at 298 K. The influences of common coexisting anions (SO_4^{2-} SiO_3^{2-}, CO_3^{2-}, PO_4^{3-} and Cl^-) and cations (Na^+, NH_4^+, K^+, Ca^{2+} and Mg^{2+}) on the removal of Sb(III) were researched at pH 4.6 ± 0.2. The concentration range of these ions was 0.1–10 mmol·L^{-1}.

2.4.4. Adsorption and Desorption Tests

To evaluate the reusability of the desired HRM@nFe$_3$O$_4$, five cycles of adsorption-desorption experiments were conducted sequentially [42]. For the adsorption experiment, 0.2 g of HRM@nFe$_3$O$_4$ was added into 1 L polyethylene bottles, which contained 1 L of 10 mg·L^{-1} Sb(III) solution at pH 4.6 ± 0.2. The solution was stirred for 4 h, and then the HRM@nFe$_3$O$_4$ after adsorption was separated from the solution by a magnet. The residual solution was sampled for the antimony concentration test. For the desorption experiment, the HRM@nFe$_3$O$_4$, which had absorbed antimony, was added into 0.5 mol·L^{-1} HCl solution and 0.5 mol·L^{-1} NaOH solution at a dosage of 4 g·L^{-1}. After agitating for 4 h, the regenerated HRM@nFe$_3$O$_4$ was separated and collected from the eluent, washed several times, dried, and prepared for the next sorption-desorption cycle.

The dose of adsorbent for all batch experiments was 0.2 g·L^{-1}. All polyethylene bottles containing mixed solution were constantly agitated at 150 rpm. At regular time intervals (10–300 min), the samples of 5 mL were immediately filtered through a 0.45 µm pore size membrane. The adsorption capacity of Sb(III) at specified time (t) was calculated by the following equation:

$$q_t = \frac{(C_0 - C_t)V}{W}, \quad (1)$$

where, q_t is the adsorption capacity (mg·g^{-1}), C_0 is the initial concentration of Sb(III) (mg·L^{-1}), C_t is the concentration of Sb(III) at specified time (t), V is the volume of the solution (L) and W is the dose of sorbent used (g).

2.5. Analytical Methods

All batch experiments were performed in the dark and repeated in triplicate. Then the concentration of residual Sb(III) in solution was analyzed using an atomic fluorescence spectrometer (AFS6500, HAIGUANG INSTRUMENT, Beijing, China). It was coupled with a hollow double cathode antimony lamp. Thiourea was used as a pre-reducing agent. The working solution was prepared with 10% HCl (GR) as the carrier solution and a mixture of 0.5% KOH and 2% KBH_4 as the reducing solution. The main current of the antimony lamp was set at 40 mA. In addition, the negative high voltage for antimony analysis was set 300 V. Argon (99.999%) was used as the shielding gas and the carrier gas, and the flow rates were

set to 800 mL·min^{-1} and 300 mL·min^{-1}, respectively. The flow rate of the liquid phase pump and the speed of the peristaltic pump were set at 1.5 mL·min^{-1} and 120 r·min^{-1}, respectively. All samples were stored in a mobile phase solution and filtered through a 0.45 μm microporous membrane. All samples were analyzed within 24 h after collection.

3. Results and Discussion

3.1. Structure, Morphology and Surface Properties of HRM@nFe$_3$O$_4$

The morphologies of HRM and HRM@nFe$_3$O$_4$ in 1:1 mass ratio were confirmed by TEM images, as seen in Figure 1. Many nanoparticles were aggregated on the surface of HRM@nFe$_3$O$_4$, with a particle size of 5 nm to 30 nm, which was much smaller than HRM. This irregular spherical shape could create porous structure and rough surface, which was the essential condition of a desired absorbent. The SEM-EDS analysis results are illustrated in Figure S1. As shown in the mapping image, Fe was evenly distributed on the surface of HRM@nFe$_3$O$_4$, and the iron content of HRM@nFe$_3$O$_4$ increased significantly compared to that of HRM. The energy image further demonstrated that the Fe mass ratio on the surface of HRM@nFe$_3$O$_4$ was about 51.93%, which was 3.7 times that of HRM. Above all, Fe was successfully loaded onto the surface of HRM in the form of small nanosized particles with non-uniform shapes [43].

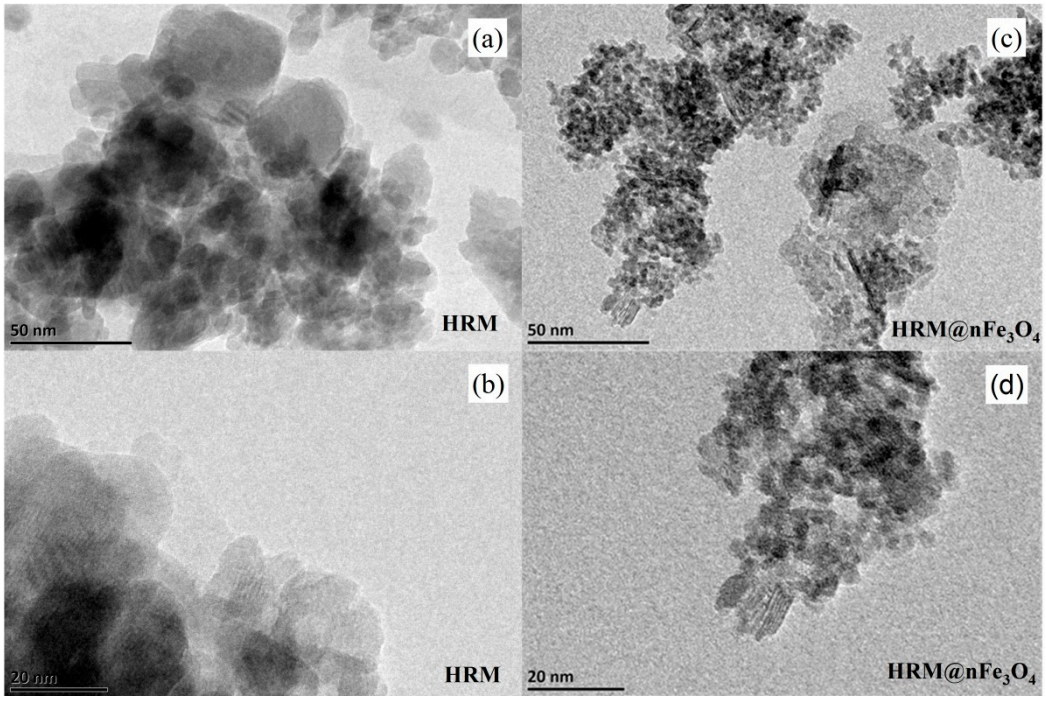

Figure 1. TEM images of HRM and HRM@nFe$_3$O$_4$: (**a**,**b**) TEM images of HRM; (**c**,**d**) TEM images of HRM@nFe$_3$O$_4$.

Figure 2 shows the XRD patterns of HRM, HRM@nFe$_3$O$_4$ and nFe$_3$O$_4$ (HRM: nFe$_3$O$_4$ with mass ratios of 1:0, 1:1 and 0:1). The pattern of HRM exhibited an unordered structure with the peaks at 24.22°, 33.22°, 35.78°, 49.62°, 54.18°, 62.66° and 64.29°, which represented the Bragg reflections from the (110), (121), (−110), (220), (132), (130) and (−211) planes, respectively, typical of Fe$_2$O$_3$ phase (Reference code: 85-0599). The HRM used in this study is rich in Fe$_2$O$_3$, and the result is identifiable to the XRF. For the synthetic nFe$_3$O$_4$, the high-intensity peaks were observed at 2θ = 30.36°, 35.76°, 43.47°, 57.51°, and 63.17° in the XRD pattern, which represented the Bragg reflections from the (220), (311), (400), (511), and (440) planes, respectively (Reference code: 75-0449). This means nFe$_3$O$_4$ was successfully loaded by the synthetic method in this study. Although some peaks could be found at 10° to 45° in the XRD pattern of the HRM@nFe$_3$O$_4$, it was difficult to distinguish the Fe$_2$O$_3$ and Fe$_3$O$_4$. In addition, there was no distinct peak at 2θ ranging from 45° to 80°, illustrating that the

original spinel structure of HRM was changed by adding nFe_3O_4, and the HRM@nFe_3O_4 was the amorphous phase. Notably, the non-crystal phase of HRM@nFe_3O_4 might result from the vigorous stirring and low-temperature drying in the synthesis procedure [44]. The performance of adsorption of HRM@nFe_3O_4 might be dependent on its amorphous structure and various functional groups on the surface. The adsorbability and surface activity of amorphous ferric oxide to antimony were demonstrated to be much stronger than that of crystalline goethite, according to the previous research [45].

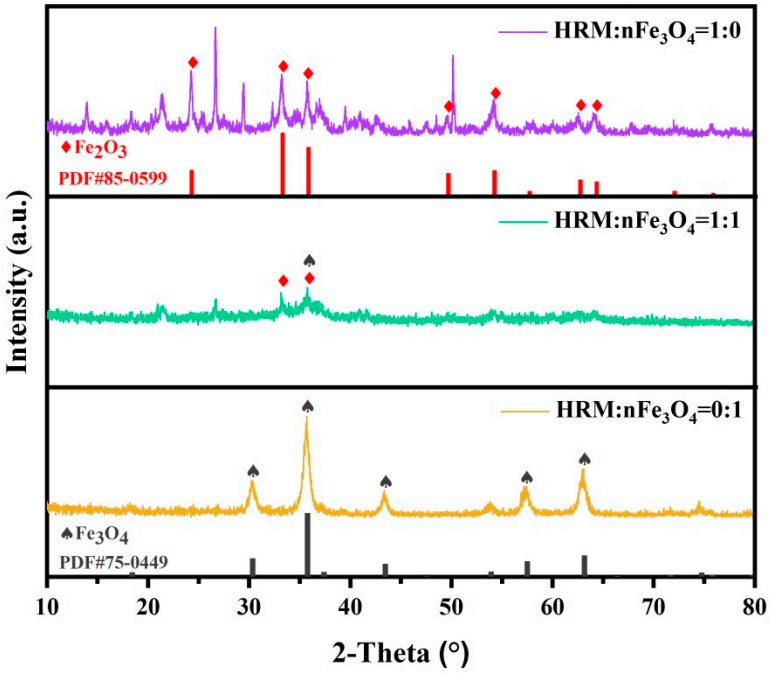

Figure 2. XRD patterns of HRM@nFe_3O_4 systems, #: Reference code.

The N_2 adsorption-desorption isotherms of HRM@nFe_3O_4 are shown in Figure S2a. They did not reach an equilibrium state at the high stage of P/P0 and presented an H3 hysteresis loop matched to type IV in isotherms classification by International Union of Pure and Applied Chemistry IUPAC. It was indicated that the existence of a slit hole structure was attributed to particle accumulation, and this material might be mesoporous adsorbent [40,46]. The BET results of HRM and HRM@nFe_3O_4 were obtained by analyzing the sorption data through the Barrett-Joyner-Halenda (BJH) model. As it showed, the HRM@nFe_3O_4 had a high specific surface area of 171.63 $m^2 \cdot g^{-1}$, average pore width of 7.62 nm and pore volume of 0.31 $cm^3 \cdot g^{-1}$, which was in the scope of mesoporous dimension and suitable for use as an absorbent. The HRM had a BET specific surface area of 15.49 $m^2 \cdot g^{-1}$, pore width of 22.76 nm and pore volume of 0.06 $cm^3 \cdot g^{-1}$. It is well-known that larger specific surface area provides more adsorption sites, while smaller particle size promotes the diffusion of small molecules from the aqueous phase onto the surface active sites [47,48].

Figure S2b illustrates the comparison of magnetic field-dependent behaviors between HRM and HRM@nFe_3O_4 in an applied magnetic field from −20 to 20 k Oe. HRM@nFe_3O_4, a kind of ferromagnetic material, showed typical hysteresis loops in magnetic behavior, with a magnetic coercivity of about 45.18 Oe, suggesting that HRM@nFe_3O_4 could be categorized as magnetically soft and possessing ferrimagnetic rather than the superparamagnetic properties. Relatively lower coercivity of HRM@nFe_3O_4 indicated a better dispersibility in the aqueous phase, because residual magnetic attraction disappeared when the external magnetic field was removed. This provided a basis for HRM@nFe_3O_4 to be a good adsorbent [37]. Apparently, the magnetic induction intensity of HRM@nFe_3O_4 was higher than that of HRM, which meant that loading nFe_3O_4 could promote the magnetiza-

tion of HRM, and the HRM@nFe_3O_4 could separate more quickly from water than HRM under an external magnetic field.

3.2. Effect of Mass Ratio of nFe_3O_4/HRM on Sb(III) Adsorption

To examine the best mass ratio of nFe_3O_4/HRM on Sb(III) adsorption, several HRM@nFe_3O_4 sorbents with different nFe_3O_4:HRM mass ratios of 0:1, 1:2, 1:1, 2:1 and 1:0 were used in Sb(III) adsorption tests. As shown in Figure 3, the adsorption capacities of various types of synthetic HRM@nFe_3O_4 were all higher than pure HRM. When the mass ratio was 1:1, the adsorption capacity was the largest, at approximately 33 $mg \cdot g^{-1}$. Hence, the nFe_3O_4 with an HRM mass ratio of 1:1 was selected as a feasible HRM@nFe_3O_4 material and applied to the following tests.

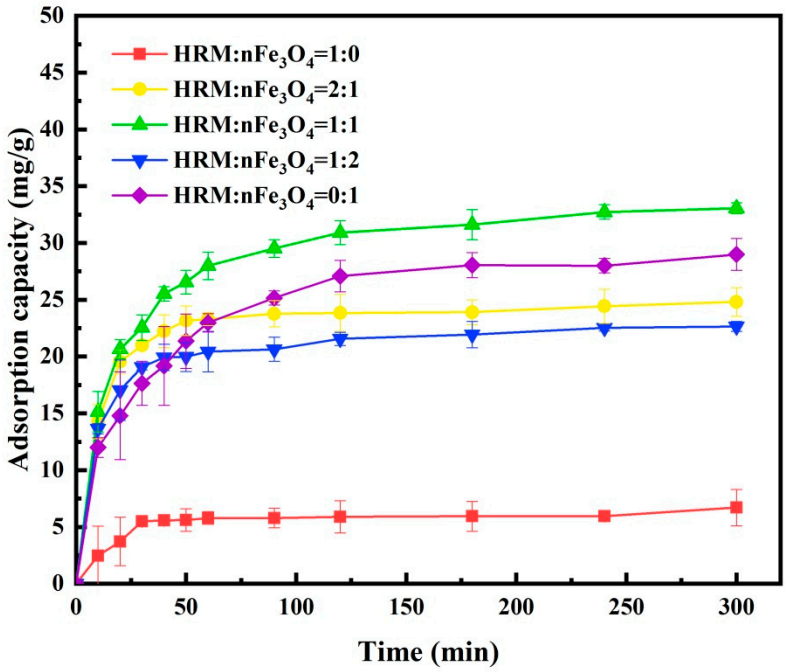

Figure 3. Effect of HRM/nFe_3O_4 mass ratio on Sb(III): initial Sb(III) concentration = 10 $mg \cdot L^{-1}$, sorbent dose = 0.2 $g \cdot L^{-1}$, pH = 4.6 ± 0.1 and T = 298 K.

3.3. Adsorption Behavior

3.3.1. Effect of Solution PH

To know the influence of electrostatic interaction on Sb(III) adsorption by HRM@nFe_3O_4, the relation between pH values and adsorption capacity was investigated, and the zeta potentials of HRM@nFe_3O_4 before and after reaction were detected. As shown in Figure 4, little effect of pH was observed on the adsorption of Sb(III) [49]. The adsorption capacity was approximately constant in the pH range from 2.6 to 11.6. It was demonstrated that there is no electrostatic attraction during the adsorption process. This is mainly due to the fact that Sb(III) exists as largely uncharged $Sb(OH)_3$ over a large pH range, from 2.0 to 10.0 [50–52], suggesting that Sb(III) could tightly bound on the surface sites via the formation of surface complexes [48]. Similar results of pH independence of Sb(III) adsorption have been reported previously for goethite and amorphous Fe hydroxides as sorbents [51,53]. The pH value results for Sb(III) solution after adsorption are illustrated in Figure 4a. It could be found that the pH value of Sb(III) solution after adsorption moved towards a pH value of 7, except for the conditions of strong acid or alkaline. This was ascribed to the idea that the corrosion of nFe_3O_4 in acid might consume H^+, while the formation of iron hydroxides in alkaline might consume OH^- [43]. The zeta potentials of HRM@nFe_3O_4 before and after reaction are shown in Figure 4b. The point of zero charge (PZC) of HRM@nFe_3O_4 shifted from 5.2 to approximately 4.8 upon Sb(III) adsorp-

tion, indicating the formation of negatively charged inner-sphere Sb(III) complexes on HRM@nFe$_3$O$_4$ [50]. Though the predominant species of aqueous Sb(III) exist as Sb(OH)$_3$ in the pH range of 2–11, the deprotonation of Sb species is likely to occur [54], as well as As [55], becoming more suitable for binding Sb(III) species present as HSbO$_2$ and Sb(OH)$_3$ when adsorbed onto the surface of metal oxides (e.g., the deprotonated form FeOSbO(OH) for Sb(III) [51,56]). The influence of pH on the sorption of Sb (III) onto HRM@nFe$_3$O$_4$ may be explained by the two following complexation mechanisms: (i) ligand exchange at the Sb center and release of hydroxides [56] and (ii) formation of a negatively charged complex [57].

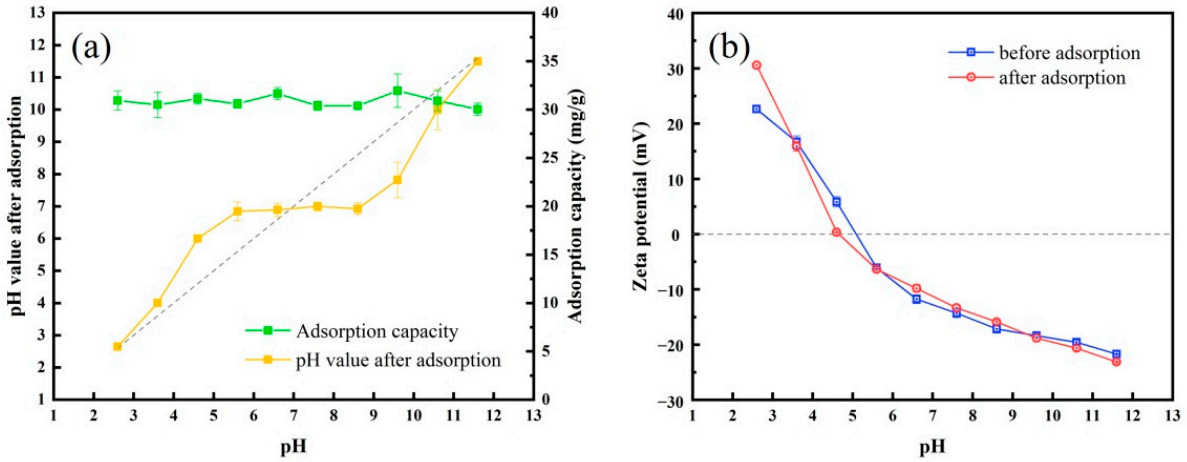

Figure 4. Sb(III) removal by HRM@nFe$_3$O$_4$ as a function of pH values and the zeta potential: (**a**) the pH value after adsorption and the adsorption capacity at different pH levels; (**b**) zeta potential before and after adsorption. Initial Sb(III) concentration = 10 mg·L^{-1}, sorbent dose = 0.2 g·L^{-1} and T = 298 K.

3.3.2. Influences of Coexisting Ions on Sb(III) Adsorption

Due to the fact that actual wastewater generally contains a variety of ions, it was necessary to understand the influence of coexisting ions on the adsorption of Sb(III) by HRM@nFe$_3$O$_4$. The influence of coexisting cations of Na^+, NH_4^+, K^+, Ca^{2+} and Mg^{2+} are shown in Figure 5a, which exhibited negligible changes on Sb(III) adsorption. The reason may be that, because Sb(III) could bind tightly to surface sites by complexation [48], Sb(III) could resist these cations during the adsorption by HRM@nFe$_3$O$_4$ [58]. It is well known that the anti-interference performance of an adsorbent is owing to the hydration radius of interference ions and the target adsorbate. The closer the hydration radius was, the stronger the competing adsorption. In this study, the hydration radius of Sb(III) was quite different from these interference cations, indicating that little adsorption process competition occurred among them [59]. The adsorption capacity of Sb(III) by HRM@nFe$_3$O$_4$ was further studied to investigate the influence of common anions of SO_4^{2-}, CO_3^{2-}, SiO_3^{2-}, PO_4^{3-} and Cl^-. As shown in Figure 5b, there was no significant effect on the absorption of Sb(III) for the anion of SO_4^{2-} and Cl^- because Sb(III) was chemisorbed onto the absorbent, whereas sulfate and chloride were mainly removed by electrostatic interaction [60]. There was no negative impact on the adsorption of Sb(III) under low anion concentrations; a slight increase was actually observed in the presence of SiO_3^{2-} and PO_4^{3-}. Similar observations have been reported in other studies, such as the removal of Sb(III) by chitosan modified iron nanosheet [48]. However, the adsorption of Sb(III) was inhibited by ions of SiO_3^{2-} and PO_4^{3-} at the concentration of 10 mmol·L^{-1}. This was because elements P and Sb are in the same main group of elements in the periodic table and have similar physicochemical properties, and thus they compete for same adsorption sites on surfaces of adsorbents [61]. It was reported in a previous study that phosphate has a huge inhibiting effect on Sb(III) adsorption [16,60]. Nevertheless, SiO_3^{2-} was anticipated to accumulate on hydrous ferric

oxides, and it was thought that the competitive adsorption with Sb(III) on HRM@nFe$_3$O$_4$ would happen [16,62,63]. On the contrary, carbonate promoted the adsorption of Sb(III), which probably can be attributed to the association between the specific adsorption of antimony on carbonate surfaces. There was significant correlation between calcium carbonate and antimony in a previous study, suggesting surface adsorption or ligand exchange with the carbonate group [64]. Furthermore, it is worth mentioning that the concentration of interference ions added in this study (10 mmol·L^{-1}) was higher than most existing in surface waters. Therefore, the adverse effects of these anions would be not seriously limit the application of HRM@nFe$_3$O$_4$.

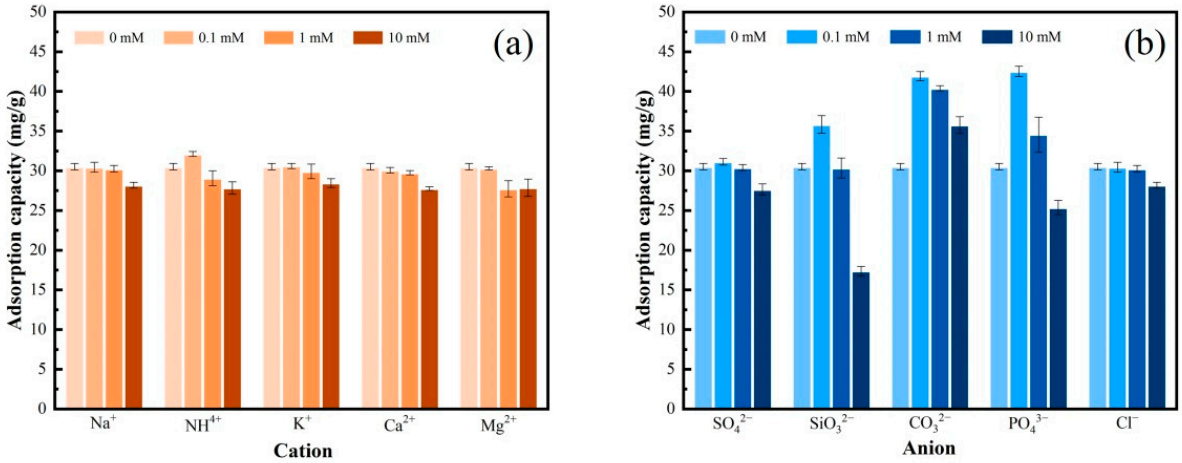

Figure 5. (**a**) Cations on the removal of Sb(III) and (**b**) anions on the removal of Sb(III). Initial Sb(III) concentration = 10 mg·L^{-1}, sorbent dose = 0.2 g·L^{-1}, pH = 4.6 ± 0.1 and T = 298 K.

3.3.3. Regeneration and Reusability of HRM@ nFe$_3$O$_4$

Reusability is one of the important indexes for evaluating the potential of an adsorbent. Therefore the recycling property of HRM@nFe$_3$O$_4$ on Sb(III) removal was studied using the adsorption capacities and the numbers of desorption cycling. The regeneration of HRM@nFe$_3$O$_4$ was desorbed after each adsorption with two different eluent of 0.5 mol·L^{-1} NaOH and 0.5 mol·L^{-1} HCl [48,65,66]. As shown in Figure S3, HRM@nFe$_3$O$_4$ retained more than 60% of the initial adsorption efficiency after the fifth adsorption–desorption cycle using NaOH as eluent, which proves the good regenerability of HRM@nFe$_3$O$_4$. The performance of NaOH was better than HCl as the eluent of HRM@nFe$_3$O$_4$. This was because NaOH might promote the oxidation of Sb(III) to Sb(V). There was still a large number of adsorption sites that could be regenerated by the ion exchange process between OH^- and $[Sb(OH)_6]^-$ on the HRM@nFe$_3$O$_4$ surface [42]. The oxidation reaction was completed within seconds, and the Sb(V) oxyanion oligomers tended to be hydrolyzed to more readily desorbed monomers [67]. There was no iron leaching at pH > 3.0, while the iron release concentration gradually increased when pH decreased to below 3.0 [39,56]. Therefore, using HCl as eluent could result in the dissolution of precipitated iron oxide during regeneration, and the procedures of solid-liquid separation inevitably cause some loss during the recovery processes. In addition, due to the adsorbed Sb(III) on materials that were not desorbed completely in previous cycles, the adsorption capacity was reduced gradually in subsequent cycles [62]. It is crucial for future studies to focus on improving the recovery rate of HRM@nFe$_3$O$_4$ for the better application of Sb(III) in wastewater treatment.

3.4. Mechanism of Sb(III) Removal by HRM@nFe$_3$O$_4$

3.4.1. Adsorption Kinetics

The kinetics of Sb(III) removal in water were investigated by batch experiments in order to acquire the adsorption rate and appropriate contact time of HRM@nFe$_3$O$_4$ in order

to understand the possible absorbed mechanism. As illustrated in Figure 6a,b, the removal of Sb(III) was very fast initially, within 60 min, reaching a plateau with 80% of Sb(III) adsorption. Over 97% of equilibrium adsorption capacity was reached after a reaction time of 240 min. The initial rapid reaction was attributed to the strong affinity sites or the precipitation of adsorbate on the surface of adsorbent [37]. The intraparticle diffusion played a dominant role in the following period [37].

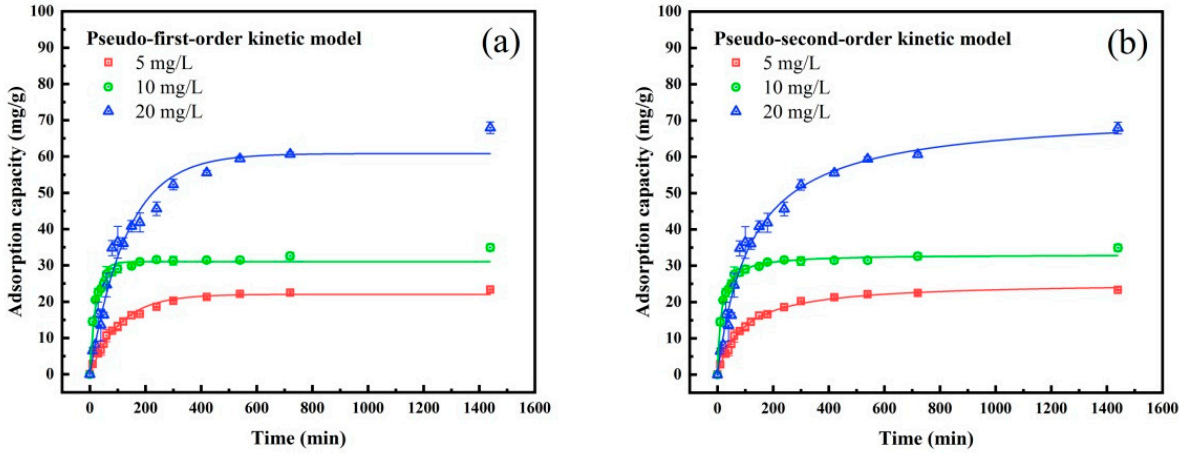

Figure 6. (**a**) The pseudo-first-order kinetic of Sb(III) sorption on HRM@nFe_3O_4 and (**b**) the pseudo-second-order kinetic of Sb(III) sorption on HRM@nFe_3O_4. Initial Sb(III) concentration = 10 g·L^{-1}, sorbent dose = 0.2 mg·L^{-1}, pH = 4.6 ± 0.1 and T = 298 K.

The kinetic data was fitted using the pseudo-first-order kinetic model equation, as follows:

$$\ln(q_e - q_t) = \ln q_e - \frac{k_1}{2.303}t, \quad (2)$$

The pseudo-second-order kinetic model equation is as follows:

$$\frac{t}{q_t} = \frac{1}{k_2 q_e^2} + \frac{t}{q_e} \quad (3)$$

where q_e is the adsorption capacity (mg·g^{-1}) of the adsorbent at equilibrium, q_t is the sorption capacity (mg·g^{-1}) at pre-selected time t (min), k_1 (min^{-1}) is the pseudo-first-order rate constant for the absorption process, and k_2 (mg·(g·min)$^{-1}$) is the pseudo-second-order rate constant. The related parameters are shown in Table 1.

Table 1. Kinetics parameters for Sb(III) sorption on HRM@nFe_3O_4.

Sb	C_0 (mg·L^{-1})	Pseudo-First-Order Model			Pseudo-Second-Order Model		
		q_e (mg·g^{-1})	k_1 (min^{-1})	R^2	q_e (mg·g^{-1})	k_2 [mg·(g·min)$^{-1}$]	R^2
	5	22.0170	0.0214	0.9838	25.4863	0.0004	0.9930
	10	31.0136	0.1013	0.9473	33.1181	0.0022	0.9909
	20	60.8113	0.0175	0.9688	72.2033	0.0001	0.9831

The above two models were employed to study the adsorption behaviors of HRM@nFe_3O_4 on Sb(III) adsorption at different initial concentrations. It was found that the pseudo-first-order model and the pseudo-second-order model were both suitable for illustrating the adsorption process of Sb(III) on HRM@nFe_3O_4. A higher correlation coefficient value (0.99) was observed using the pseudo-second model. This demonstrates that the adsorption process of Sb(III) by HRM@nFe_3O_4 was related to chemical adsorption and physical adsorption [44] and that chemisorption might play a major role in the reaction process [8].

The pseudo-second order kinetic model also presented a better fitting degree at lower Sb(III) concentration. This indicates that the process of removing Sb(III) by HRM@nFe_3O_4 resulted from a multi-mechanism synergy [43].

3.4.2. Adsorption Isotherms

The two classical Langmuir and Freundlich models were employed to study the adsorption isotherms and calculate the maximum adsorption capacities of the materials at 298 K, 308 K and 318 K. The resulting data were analyzed with the Langmuir equation:

$$\frac{c_e}{q_e} = \frac{c_e}{q_m} + \frac{1}{q_m k_L}, \quad (4)$$

and the Freundlich equation:

$$\log q_e = \frac{1}{n} \log c_e + \log k_F, \quad (5)$$

where c_e (mg·L^{-1}) is the concentration of Sb(III) at equilibrium, q_e (mg·g^{-1}) is the equilibrium adsorption capacity of Sb(III), q_m (mg·g^{-1}) is the maximum absorption amount of the Sb(III), k_L (L·mg^{-1}) is the Langmuir equilibrium sorption constant, k_F (L·mg^{-1}) is the Freundlich characteristic constant, which is proportional to the equilibrium constant, and n is the index of adsorption strength, where a lower value indicates more homogeneous surfaces.

Adsorption isotherm data explored by nonlinear fitting of the Langmuir model and Freundlich model is shown in Figure 7a,b. Related isotherm parameters that were calculated are summarized in Table 2. Better correlation coefficients (R^2 values of 0.9967, 0.9948 and 0.9946) fitted using the Langmuir model were obtained in this work. On the basis of the Langmuir model, the adsorbent surface was homogeneous, which was in connection with uniform monolayer adsorption onto the surface of the adsorbent, including a limited number of adsorption sites. Meanwhile, maximum adsorption capacity was obtained when all adsorption sites on the adsorbent were occupied as single layer [41]. The maximum adsorption capacity of Sb(III) on HRM@nFe_3O_4 was 98.03 mg·g^{-1} at 308 K, in theory, according to the nonlinear Langmuir model. Normally, the adsorptive action occurs easily when n is larger than 2.0, while it is unlikely to occur when n is below 0.5 [68]. The values of n were 3.16, 3.24 and 3.56, as seen in Table 2, indicating that Sb(III) was easily adsorbed on HRM@nFe_3O_4, which was attributed to the large number of adsorption sites on the surface. The performance comparison between HRM@nFe_3O_4 and various adsorbents for the removal of Sb(III) is shown in the Table S2. As can be seen, the maximum adsorption capacity was larger than carbon nanofibers decorated with ZrO_2 (ZrO_2 -MWCNT) [4] and a zirconium metal-organic framework modified amino (UiO-66(NH_2)) [69], the dosage of HRM@nFe_3O_4 was lower than Fe(0)-Zeolite [70], Praphene was modified with polyamide composite sorbent (PAG) [66] and three-dimensional Cu(II)-specific metallogels (Cu-MG) [49], and the pH range was wider. Furthermore, the equilibration time of HRM@nFe_3O_4 was shorter than polyacrylonitrile modified by an ultrahigh percentage of amidoxime groups (UAPAN) [68] and NU-1000 [52]. It can be found that HRM@nFe_3O_4 is superior to many published adsorbents.

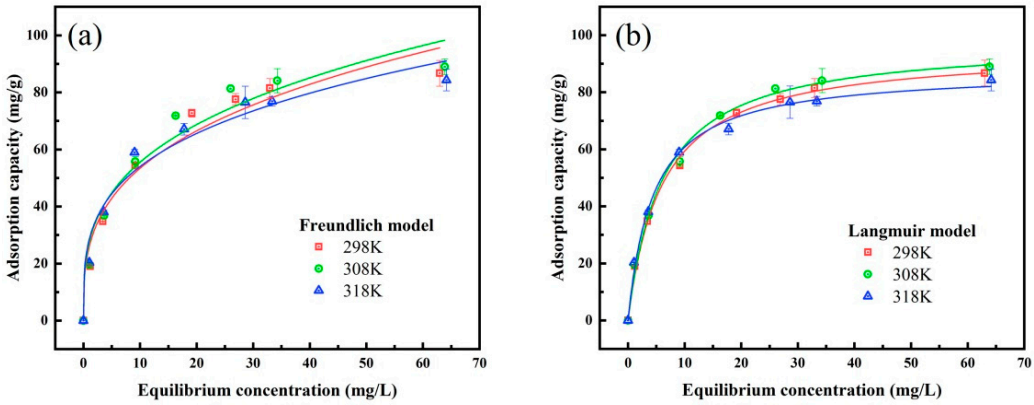

Figure 7. (**a**) The adsorption isotherm of Sb(III) in Langmuir model and (**b**) the adsorption isotherm of Sb(III) in Freundlich model. Initial concentration of Sb(III) = 5–80 mg·L^{-1}, sorbent dose = 200 mg·L^{-1}, pH = 4.6 ± 0.1 and T = 298 K.

Table 2. Isotherm parameters for Sb(III) sorption on HRM@nFe_3O_4.

Sb	T (K)	Langmuir Model			Freundlich Model		
		k_L (L·mg^{-1})	q_m (mg·g^{-1})	R^2	k_F (L·mg^{-1})	n	R^2
	298	0.1661	95.0291	0.9967	25.7512	3.1579	0.9598
	308	0.1665	98.0278	0.9948	27.2642	3.2412	0.9557
	318	0.2249	87.7352	0.9946	28.2786	3.5599	0.9652

3.4.3. Influence of Functional Groups

The FTIR spectra of HRM@nFe_3O_4 before and after Sb(III) adsorption were recorded to study the adsorption mechanisms. As shown in Figure S4, the band at 460 cm^{-1} was ascribed to Fe-O vibrational transition [65], and the band became broader but less intense after loading nFe_3O_4 on HRM. This indicates that a new, different Fe-O band emerged [70]. The peak of CH_2, at 993 cm^{-1}, saw surface distortion vibration, which disappeared after modification. A minor new peak was found at 918 cm^{-1} for HRM@nFe_3O_4, which resulted from the -OH group on the surface of absorbent, as recorded in previous studies [71]. Vibration peak appeared at 1384 cm^{-1}, which was -COO-; symmetrical stretching was changed after loading nFe_3O_4, but it kept consistent shape after adsorption [54,72]. This suggested that doping nFe_3O_4 changed the functional groups related to -COO-, but these functional groups did not participate in the removal of Sb(III). The peak of 1635 cm^{-1} was stronger after HRM was modified by nFe_3O_4, but was not obviously changed after the adsorption of Sb(III) [47,70,73]. It can be found that strong band at 3420 cm^{-1} (O-H stretching vibration) weakened after adsorption, indicating that the hydroxyl groups on the absorbent surface were involved in the Sb(III) adsorption [40,74].

3.4.4. Adsorption Mechanism Reconstruction

The chemical compositions of HRM and HRM@nFe_3O_4 before and after Sb(III) sorption were further examined by XPS. As displayed in XPS survey spectra in Figure 8a, the HRM@nFe_3O_4 after Sb(III) adsorption presented the characteristic peaks of C1s, O1s, Fe2p, Sb3d3 and Sb4d, while HRM and HRM@nFe_3O_4 only showed the characteristic peaks of C1s, O1s and Fe2p. The emergence of Sb3d3 and Sb4d peaks were observed after Sb(III) adsorption, suggesting the successful attachment of Sb(III) on the surface of HRM@nFe_3O_4. The intensity of Fe2p peaks was much weaker in HRM than that in HRM@nFe_3O_4 because of the lower Fe content, which was in agreement with EDS results. The C1s spectrum of HRM@nFe_3O_4 was differentiated into three peaks at binding energies of 284.8, 286.4 and 288.4 eV, corresponding to C=C, C-O and C=O bonds, respectively [4]. As shown in Figure 8b, the peaks of carbon were hardly shifted after modification by nFe_3O_4, but the

peak area ratio of C-O and C=O was increased. This proved that the chemical environment around carbon was changed after adding nFe_3O_4 [62].

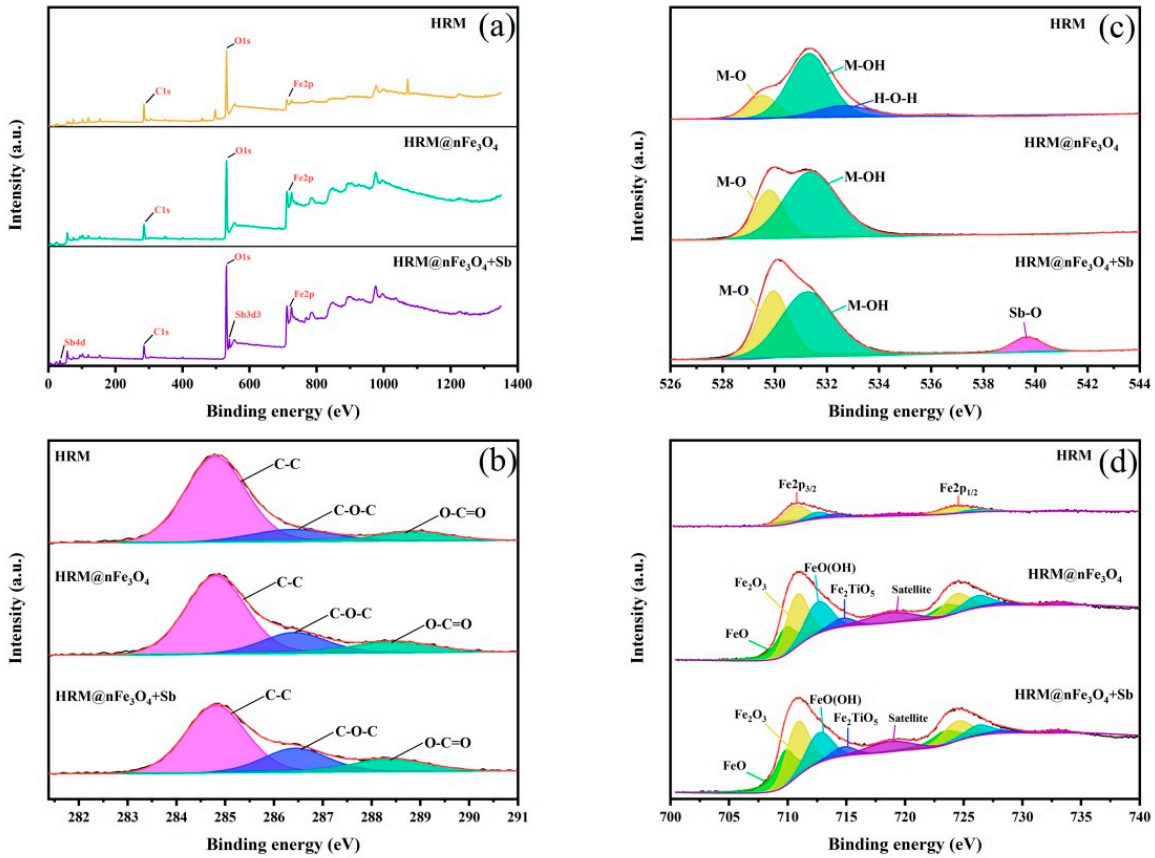

Figure 8. XPS spectra of HRM, HRM@nFe_3O_4 and HRM@nFe_3O_4 after Sb(III) sorption: (**a**) the XPS survey spectra, (**b**) C 1s spectra, (**c**) O1s spectra and (**d**) Fe2p spectra.

According to the binding energy for different species of oxygen with metal (M), the O1s and Sb3p spectrum was used to study the changes of components specifically. As shown in Figure 8c, the peaks at 532.6 eV, 531.3 eV, 529.5 eV and 539.9 eV corresponded to the H-O-H, M-OH, M-O and Sb-O bonds, respectively [4,43]. Because HRM contains many metal oxides, M-O and M-OH did not carry out peak separation specifically. However, due to the high iron content of HRM, it could be inferred that Fe-O-Fe and Fe-OH played the leading role in M-O and M-OH. The percentages of M-O, M-OH and H-O-H in HRM were 17.91%, 64.38% and 17.71%, respectively. After loading nFe_3O_4, the content of M-O in HRM@nFe_3O_4 increased to 70.64%, and M-OH to 29.36%, but H-O-H disappeared. However, the adsorbed H_2O did not participate in the reaction between absorption [4,75]. This could indicate that the nFe_3O_4 was synthetized successfully with some byproducts of M-OH, such as FeOOH. After adsorption of Sb(III), the contents of M-O increased to 35.28%, whereas that of M-OH decreased to 56.99%, because M-OH and Sb formed M-O-Sb complexes by surface complexation [45,47,56,76]. Furthermore, the peaks of the M-OH shifted to higher binding energies after Sb(III) adsorption, which could also demonstrate the interaction between M-OH and Sb(III) [40]. This was consistent with the result obtained by FT-IR. Moreover, the fitted characteristic peak for O1s at 539.9 eV corresponded to Sb(III)-O after reaction, which provided supportive evidence for the attachment of Sb(III) on HRM@nFe_3O_4 [52,62,63]. Meanwhile, the -OH group on HRM@nFe_3O_4 might be partially substituted by Sb species during the antimony adsorption process, thus leading to the formation of inner-sphere surface complexes.

As illustrated in Figure 8d, the binding energy of Fe2p3/2 at 712.4–712.7 eV and that of Fe2p1/2 at 726.2–726.3 eV were ascribed to FeO(OH) [77]. The binding energy at 710.6–710.8eV and 724.3–724.4 eV were characteristic of Fe_2O_3 [48,78]. Extra Fe(III) double peaks were observed at 714.5–714.8 eV and 726.0–726.3 eV, which were attributed to Fe_2TiO_5 [79,80]. Because FeO is known to be extremely unstable, the peaks at 709.6–709.9 eV and 723.1–723.4 eV might belong to the Fe(II) oxidation state in Fe_3O_4. Moreover, there were two satellite peaks located at 718.7–718.8 eV and 732.7–733.2 eV. The binding energy and peak shape of Fe2p were almost unchanged after the adsorption, implying that the chemical valence of Fe stayed the same [45]. Fe_2O_3 was the main iron compound in HRM, with tiny amounts of FeO(OH) and Fe_3O_4. After the modification of loading nFe_3O_4, the content of FeO was increased from about 1.2% to 27.3%, and FeO(OH) was raised from 20.3% to 27.4%, but Fe_2O_3 decreased from 61.4% to 38.7%, and Fe_2TiO_5 decreased from 17.2% to 6.5%. This indicated that nFe_3O_4 was successfully loaded on the surface of HRM, and the by-product of nFe_3O_4 synthesized by this method was FeO(OH). This may indicate compounds whose chemical formula is likely to be $3Fe_2O_3{\cdot}FeO(OH){\cdot}4H_2O$ [81]. The instability of amorphous ferrihydrite drove it into highly stable and crystalline goethite and lepidocrocite [45]. Comparing the before and after adsorption, it was found that the rate of Fe_2TiO_5 changed negligibly, the rate of FeO(OH) decreased to 23.1% and Fe_2O_3 decreased to 37.9%, while the rate of FeO increased to 32.5% after the sorption of Sb(III). This phenomenon can be explained by the fact that there was a certain loss of HRM during the magnetic recovery process due to its nonmagnetic and hydrophilic ingredients. In addition, the reduction of FeO(OH) was not only a result of the loss of HRM@nFe_3O_4 but also due to the strong interactions between FeO(OH) and Sb(III), which is consistent with previous results [62].

Accordingly, the generation of nFe_3O_4 and its iron-compound by-products were determined as detailed in the following equations:

$$Fe^{3+} + 2H_2O \xrightarrow{OH^-} FeO(OH) + 3H^+$$

$$Fe^{2+} + Fe^{3+} + 5OH^- \xrightarrow{N_2} Fe(OH)_2 + Fe(OH)_3$$

$$4Fe(OH)_2 + O_2 \rightarrow FeO(OH) + 2H_2O$$

$$Fe(OH)_2 + 3Fe(OH)_3 \xrightarrow{N_2} FeO(OH) + Fe_3O_4 + 5H_2O$$

$$4Fe_3O_4 + 6H_2O + O_2 \rightarrow 12FeO(OH)$$

The formation of FeO(OH) could be attributed mainly to hydrolysis of $FeCl_3$ [82,83], the complexation of $Fe(OH)_2$ with $Fe(OH)_3$, as well as the oxidation of $Fe(OH)_2$ and Fe_3O_4 [32]. Hence, abundant surface groups and active sites were available after modification by nFe_3O_4.

The potential adsorption mechanisms between Sb(III) and HRM@nFe_3O_4 are shown in Figure 9. It is obvious that Sb was chemically bonded with Fe from the XPS analysis, which was coincident with the results of sorption isotherms and sorption kinetics. Additionally, the larger specific surface area (S_{BET}) on HRM@nFe_3O_4 indicated that there were more active sites and better antimony adsorption performance. Furthermore, surface complexation reaction between Sb(III) and amorphous ferric oxide, including nFe_3O_4 and its by-products FeO(OH) and $Fe(OH)_3$, played an indispensable role in the removal of Sb(III) by HRM@nFe_3O_4. Hydrogen bonds between hydroxyl groups on HRM@nFe_3O_4 and antimony molecules were also conductive to the removal of Sb(III) [37,43]. Moreover, a small number of corrosion products of HRM@nFe_3O_4 produced by Fe^{3+} could remove Sb(III) from the aqueous phase by co-precipitation [43,84]. It is reasonable to speculate that the loading of nFe_3O_4 changed the surface structure and the functional groups such that the adsorption capacity was improved eventually.

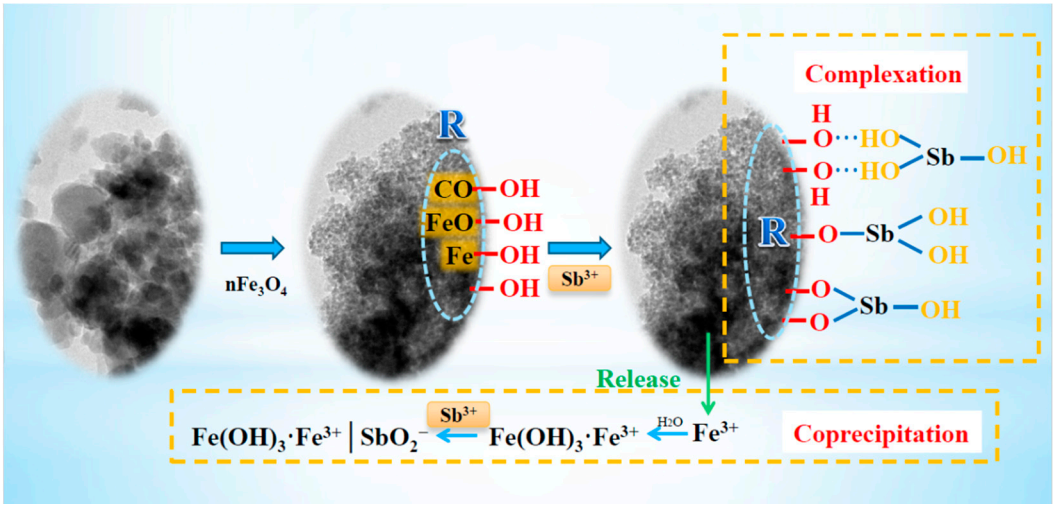

Figure 9. Proposed mechanisms for the adsorption of Sb(III) onto HRM@nFe_3O_4.

4. Conclusions

In this work, the HRM functionalized with nFe_3O_4 was synthesized by the co-precipitation method, which showed favorable physical and chemical characteristics and adsorption performance. The adsorption capacity of HRM@nFe_3O_4 was significantly improved compared with HRM. The adsorption of Sb(III) was not limited by the solution pH. Most of coexisting cations and anions showed negligible interference on Sb(III) removal. The XRD, TEM, SEM, BET, FTIR and XPS analysis demonstrated that nFe_3O_4 particles were loaded on the surface of HRM successfully. The addition of nFe_3O_4 endowed HRM@nFe_3O_4 with magnetic performance, enhancing the efficiency of solid-liquid separation. After loading nFe_3O_4, the generation of iron oxides and hydroxides played a significant role in the Sb(III) removal. According to the results of batch experiments and characterization analysis, the major mechanisms of removing Sb(III) were complexation and co-precipitation. The great Sb(III) adsorption performance illustrated that the novel HRM functionalized nFe_3O_4 shows great potential in the wastewater treatment field, with the properties of high efficiency, simple fabrication, wide suitability range of pH, good recyclability and low cost.

Supplementary Materials: The following are available online at https://www.mdpi.com/2073-4441/13/6/809/s1, Figure S1: SEM-EDS spectrum and Fe-mapping images of HRM and HRM@nFe_3O_4: (a) Fe-mapping images of HRM, (b) Fe-mapping images of HRM@nFe_3O_4, (c) EDS spectrum images of HRM and (d) SEM-EDS spectrum images of HRM@nFe_3O_4; Figure S2: (a) N_2 adsorption-desorption isotherms of HRM@nFe_3O_4 and (b) magnetization versus applied magnetic field for HRM and HRM@nFe_3O_4; Figure S3: Sb(III) sorption and desorption in five consecutive cycles for HRM@nFe_3O_4. Sorption conditions: initial Sb(III) concentration = 10 mg·L^{-1}, sorbent dose = 0.2 g·L^{-1}, pH = 4.6 ± 0.1, T = 298 K and contact time = 4 h. Desorption conditions: regenerant = 0.5 mol·L^{-1} HCl or NaOH, dose = 4 g·L^{-1}, T = 298 K and contact time = 4 h; Figure S4: FTIR spectra of initial HRM, HRM@nFe_3O_4 and HRM@nFe_3O_4 after Sb(III) sorption; Table S1: Compositional matrix of the red mud (X-ray fluorescence data); Table S2: Comparison of adsorption capacity of Sb(III) by the synthesized HRM@nFe_3O_4 sorbent with different sorbents.

Author Contributions: Conceptualization, Y.P. and Y.Y.; methodology, Y.P. and Q.M.; software, Y.P.; validation, Y.P., Y.Y. and L.L.; formal analysis, S.L. and Y.Z.; investigation, S.L. and Y.Y.; resources, Q.M. and J.Y.; data curation, Y.Y. and K.P.; writing—original draft preparation, Y.P.; writing—review and editing, L.L. and S.L.; visualization, K.P.; supervision, L.L. and Y.Y.; project administration, L.L.; funding acquisition, L.L., S.L. and Y.Y. All authors have read and agreed to the published version of the manuscript.

Funding: This research was funded by the National Natural Science Foundation of China, grant number 42077380, Hunan Provincial Key R&D, grant number 2019SK2281 and 2019WK2031, National Key R&D Projects of China, grant number 2016YFC0403002, Research Foundation of Education Bureau of Hunan Province, grant number 20A239 and the National Natural Science Foundation of Hunan Province, grant number 2020JJ5227.

Institutional Review Board Statement: The study was conducted according to the guidelines on experimental ethical provisions and welfare of animals enforced by the European Union and was coordinated by J.M. Santos, who holds FELASA level C certification (www.felasa.eu accessed on 2 February 2021) to direct animal experiments. Fish experiments and maintenance in the laboratory and experimental facility were authorized (reference DGAV: 0420/000/000/2012) by the Department for Health and Animal Protection (Direcção de Serviços de Saúde e Protecção Animal) in accordance with the recommendations of the "Protection of animal use for experimental and scientific work". Fishing and handling permits for capture of wild fish (96/2018/CAPT, 97/2018/CAPT, and 98/2018/CAPT) were issued by the Portuguese Institute for Nature Conservation and Forests (ICNF, I.P.).

Data Availability Statement: Not applicable.

Acknowledgments: The authors would like to thank the anonymous reviewers for their valuable comments and suggestions on previous versions of this paper.

Conflicts of Interest: The authors declare no conflict of interest.

References

1. Feng, R.; Lei, L.; Su, J.; Zhang, R.; Zhu, Y.; Chen, W.; Wang, L.; Wang, R.; Dai, J.; Lin, Z.; et al. Toxicity of different forms of antimony to rice plant: Effects on root exudates, cell wall components, endogenous hormones and antioxidant system. *Sci. Total Environ.* **2020**, *711*, 134589. [CrossRef]
2. Shan, J.; He, M.; Lin, C.; Ouyang, W.; Liu, X. Simultaneous electrochemical determination of Sb(III) and Sb(V) in Water samples: Deposition potential differences and Sb(III) photooxidation characteristics. *Sens. Actuators B Chem.* **2020**, *305*, 127454. [CrossRef]
3. Yang, X.; Shi, Z.; Yuan, M.; Liu, L. Adsorption of Trivalent Antimony from Aqueous Solution Using Graphene Oxide: Kinetic and Thermodynamic Studies. *J. Chem. Eng. Data* **2015**, *60*, 806–813. [CrossRef]
4. Luo, J.; Luo, X.; Crittenden, J.C.; Qu, J.; Bai, Y.; Peng, Y.; Li, J. Removal of Antimonite (Sb(III)) and Antimonate (Sb(V)) from Aqueous Solution Using Carbon Nanofibers That Are Decorated with Zirconium Oxide (ZrO2). *Environ. Sci. Technol.* **2015**, *49*, 11115–11124. [CrossRef] [PubMed]
5. Filella, M.; Belzile, N.; Chen, Y.-W. Antimony in the environment: A review focused on natural waters: II. Relevant solution chemistry. *Earth-Sci. Rev.* **2002**, *59*, 265–285. [CrossRef]
6. Winship, K. Toxicity of antimony and its compounds. *Advers. Drug React. Acute Poisoning Rev.* **1987**, *6*, 67–90.
7. U.S. Environmental Protection Agency. *Drinking Water Standards and Health Advisories*; Office of Water: Washington, DC, USA, 2009.
8. Guo, W.; Fu, Z.; Zhang, Z.; Wang, H.; Liu, S.; Feng, W.; Zhao, X.; Giesy, J.P. Synthesis of Fe_3O_4 magnetic nanoparticles coated with cationic surfactants and their applications in Sb(V) removal from water. *Sci. Total Environ.* **2020**, *710*, 136302. [CrossRef]
9. Guo, X.; Wu, Z.; He, M. Removal of antimony(V) and antimony(III) from drinking water by coagulation–flocculation–sedimentation (CFS). *Water Res.* **2009**, *43*, 4327–4335. [CrossRef]
10. Wu, Z.; He, M.; Guo, X.; Zhou, R. Removal of antimony (III) and antimony (V) from drinking water by ferric chloride coagulation: Competing ion effect and the mechanism analysis. *Sep. Purif. Technol.* **2010**, *76*, 184–190. [CrossRef]
11. Wu, F.; Sun, F.; Wu, S.; Yan, Y.; Xing, B. Removal of antimony(III) from aqueous solution by freshwater cyanobacteria Microcystis biomass. *Chem. Eng. J.* **2012**, *183*, 172–179. [CrossRef]
12. Naiya, T.K.; Bhattacharya, A.K.; Das, S.K. Adsorption of Cd (II) and Pb (II) from aqueous solutions on activated alumina. *J. Colloid Interface Sci.* **2009**, *333*, 14–26. [CrossRef]
13. Wang, X.; He, M.; Lin, C.; Gao, Y.; Zheng, L. Antimony(III) oxidation and antimony(V) adsorption reactions on synthetic manganite. *Geochemistry* **2012**, *72*, 41–47. [CrossRef]
14. Bergmann, M.H.; Koparal, A.S. Electrochemical antimony removal from accumulator acid: Results from removal trials in laboratory cells. *J. Hazard. Mater.* **2011**, *196*, 59–65. [CrossRef] [PubMed]
15. Sun, W.; Xiao, E.; Dong, Y.; Tang, S.; Krumins, V.; Ning, Z.; Sun, M.; Zhao, Y.; Wu, S.; Xiao, T. Profiling microbial community in a watershed heavily contaminated by an active antimony (Sb) mine in Southwest China. *Sci. Total Environ.* **2016**, *550*, 297–308. [CrossRef]
16. Wei, D.; Li, B.; Luo, L.; Zheng, Y.; Huang, L.; Zhang, J.; Yang, Y.; Huang, H. Simultaneous adsorption and oxidation of antimonite onto nano zero-valent iron sludge-based biochar: Indispensable role of reactive oxygen species and redox-active moieties. *J. Hazard. Mater.* **2020**, *391*, 122057. [CrossRef]
17. Ungureanu, G.; Santos, S.; Boaventura, R.; Botelho, C. Arsenic and antimony in water and wastewater: Overview of removal techniques with special reference to latest advances in adsorption. *J. Environ. Manag.* **2015**, *151*, 326–342. [CrossRef]

18. Bray, A.W.; Stewart, D.I.; Courtney, R.; Rout, S.P.; Humphreys, P.N.; Mayes, W.M.; Burke, I.T. Sustained bauxite residue rehabilitation with gypsum and organic matter 16 years after initial treatment. *Environ. Sci. Technol.* **2018**, *52*, 152–161. [CrossRef]
19. Zhou, R.; Liu, X.; Luo, L.; Zhou, Y.; Wei, J.; Chen, A.; Tang, L.; Wu, H.; Deng, Y.; Zhang, F.; et al. Remediation of Cu, Pb, Zn and Cd-contaminated agricultural soil using a combined red mud and compost amendment. *Int. Biodeterior. Biodegrad.* **2017**, *118*, 73–81. [CrossRef]
20. Li, G.; Liu, M.; Rao, M.; Jiang, T.; Zhuang, J.; Zhang, Y. Stepwise extraction of valuable components from red mud based on reductive roasting with sodium salts. *J. Hazard. Mater.* **2014**, *280*, 774–780. [CrossRef]
21. Lyu, F.; Gao, J.; Sun, N.; Liu, R.; Sun, X.; Cao, X.; Wang, L.; Sun, W. Utilisation of propyl gallate as a novel selective collector for diaspore flotation. *Miner. Eng.* **2019**, *131*, 66–72. [CrossRef]
22. Zhang, T.; Wang, K.; Liu, Y.; Lyu, G.; Li, X.; Chen, X. A Review of Comprehensive Utilization of High-Iron Red Mud of China. *Light Met.* **2020**, 65–71. [CrossRef]
23. Power, G.; Gräfe, M.; Klauber, C. Bauxite residue issues: I. Current management, disposal and storage practices. *Hydrometallurgy* **2011**, *108*, 33–45. [CrossRef]
24. Ke, W.; Zhang, X.; Zhu, F.; Wu, H.; Zhang, Y.; Shi, Y.; Hartley, W.; Xue, S. Appropriate human intervention stimulates the development of microbial communities and soil formation at a long-term weathered bauxite residue disposal area. *J. Hazard. Mater.* **2021**, *405*, 124689. [CrossRef]
25. Khairul, M.; Zanganeh, J.; Moghtaderi, B. The composition, recycling and utilisation of Bayer red mud. *Resour. Conserv. Recycl.* **2019**, *141*, 483–498. [CrossRef]
26. Li, H.; Liu, Y.; Zhou, Y.; Zhang, J.; Mao, Q.; Yang, Y.; Huang, H.; Liu, Z.; Peng, Q.; Luo, L. Effects of red mud based passivator on the transformation of Cd fraction in acidic Cd-polluted paddy soil and Cd absorption in rice. *Sci. Total Environ.* **2018**, *640-641*, 736–745. [CrossRef]
27. Hua, Y.; Heal, K.V.; Friesl-Hanl, W. The use of red mud as an immobiliser for metal/metalloid-contaminated soil: A review. *J. Hazard. Mater.* **2017**, *325*, 17–30. [CrossRef]
28. Wang, L.; Hu, G.; Lyu, F.; Yue, T.; Tang, H.; Han, H.; Yang, Y.; Liu, R.; Sun, W. Application of Red Mud in Wastewater Treatment. *Minerals* **2019**, *9*, 281. [CrossRef]
29. Li, H.; Liu, L.; Luo, L.; Liu, Y.; Wei, J.; Zhang, J.; Yang, Y.; Chen, A.; Mao, Q.; Zhou, Y. Response of soil microbial communities to red mud-based stabilizer remediation of cadmium-contaminated farmland. *Environ. Sci. Pollut. Res.* **2018**, *25*, 11661–11669. [CrossRef] [PubMed]
30. Wu, C.; Huang, L.; Xue, S.-G.; Huang, Y.-Y.; Hartley, W.; Cui, M.-Q.; Wong, M.-H. Arsenic sorption by red mud-modified biochar produced from rice straw. *Environ. Sci. Pollut. Res.* **2017**, *24*, 18168–18178. [CrossRef]
31. Yoon, K.; Cho, D.W.; Tsang, Y.F.; Tsang, D.C.; Kwon, E.E.; Song, H. Synthesis of functionalised biochar using red mud, lignin, and carbon dioxide as raw materials. *Chem. Eng. J.* **2019**, *361*, 1597–1604. [CrossRef]
32. Li, Y.; Huang, H.; Xu, Z.; Ma, H.; Guo, Y. Mechanism study on manganese(II) removal from acid mine wastewater using red mud and its application to a lab-scale column. *J. Clean. Prod.* **2020**, *253*, 119955. [CrossRef]
33. Chon, C.-M.; Cho, D.-W.; Nam, I.-H.; Kim, J.-G.; Song, H. Fabrication of Fe/Mn oxide composite adsorbents for adsorptive removal of zinc and phosphate. *J. Soils Sediments* **2018**, *18*, 946–956. [CrossRef]
34. Nizamuddin, S.; Siddiqui, M.; Mubarak, N.; Baloch, H.A.; Abdullah, E.; Mazari, S.A.; Griffin, G.; Srinivasan, M.; Tanksale, A. Iron Oxide Nanomaterials for the Removal of Heavy Metals and Dyes from Wastewater. *Nanoscale Mater. Water Purif.* **2019**, 447–472. [CrossRef]
35. Hu, Y.; Peng, X.; Ai, Z.; Jia, F.; Zhang, L. Liquid Nitrogen Activation of Zero-Valent Iron and Its Enhanced Cr(VI) Removal Performance. *Environ. Sci. Technol.* **2019**, *53*, 8333–8341. [CrossRef] [PubMed]
36. Wang, H.; He, Y.; Chai, L.; Lei, H.; Yang, W.; Hou, L.; Yuan, T.; Jin, L.; Tang, C.J.; Luo, J. Highly-dispersed Fe_2O_3 @Celectrode materials for Pb2+ removal by capacitive deionization. *Carbon* **2019**, *153*, 12–20. [CrossRef]
37. Qi, Z.; Joshi, T.P.; Liu, R.; Liu, H.; Qu, J. Synthesis of Ce(III)-doped Fe_3O_4 magnetic particles for efficient removal of antimony from aqueous solution. *J. Hazard. Mater.* **2017**, *329*, 193–204. [CrossRef]
38. Qi, P.; Luo, R.; Pichler, T.; Zeng, J.; Wang, Y.; Fan, Y.; Sui, K. Development of a magnetic core-shell Fe_3O_4@TA@UiO-66 microsphere for removal of arsenic(III) and antimony(III) from aqueous solution. *J. Hazard. Mater.* **2019**, *378*, 120721. [CrossRef] [PubMed]
39. Hao, H.; Liu, G.; Wang, Y.; Shi, B.; Han, K.; Zhuang, Y.; Kong, Y. Simultaneous cationic Cu (II)-anionic Sb (III) removal by NH2-Fe3O4-NTA core-shell magnetic nanoparticle sorbents synthesized via a facile one-pot approach. *J. Hazard. Mater.* **2019**, *362*, 246–257. [CrossRef]
40. Yu, G.; Fu, F. Exploration of different adsorption performance and mechanisms of core-shell Fe_3O_4@Ce-Zr oxide composites for Cr(VI) and Sb(III). *J. Colloid Interface Sci.* **2020**, *576*, 10–20. [CrossRef]
41. Zhang, J.; Deng, R.J.; Ren, B.Z.; Hou, B.; Hursthouse, A. Preparation of a novel Fe_3O_4/HCO composite adsorbent and the mechanism for the removal of antimony (III) from aqueous solution. *Sci. Rep.* **2019**, *9*, 13021. [CrossRef]
42. Wang, L.; Wang, J.; Wang, Z.; He, C.; Lyu, W.; Yan, W.; Yang, L. Enhanced antimonate (Sb(V)) removal from aqueous solution by La-doped magnetic biochars. *Chem. Eng. J.* **2018**, *354*, 623–632. [CrossRef]
43. Liu, S.; Feng, H.; Tang, L.; Dong, H.; Wang, J.; Yu, J.; Feng, C.; Liu, Y.; Luo, T.; Ni, T. Removal of Sb(III) by sulfidated nanoscale zerovalent iron: The mechanism and impact of environmental conditions. *Sci. Total Environ.* **2020**, *736*, 139629. [CrossRef]

44. Zhang, W.; Liu, C.; Zheng, T.; Ma, J.; Zhang, G.; Ren, G.; Wang, L.; Liu, Y. Efficient oxidation and sorption of arsenite using a novel titanium(IV)-manganese(IV) binary oxide sorbent. *J. Hazard. Mater.* **2018**, *353*, 410–420. [CrossRef] [PubMed]
45. Yang, K.; Zhou, J.; Lou, Z.; Zhou, X.; Liu, Y.; Li, Y.; Baig, S.A.; Xu, X. Removal of Sb(V) from aqueous solutions using Fe-Mn binary oxides: The influence of iron oxides forms and the role of manganese oxides. *Chem. Eng. J.* **2018**, *354*, 577–588. [CrossRef]
46. Sing, K.S.W. Reporting Physisorption Data for Gas Solid Systems with Special Reference to the Determination of Surface-Area and Porosity. *Pure Appl. Chem.* **1985**, *57*, 603–619. [CrossRef]
47. Chen, J.; Wang, J.; Zhang, G.; Wu, Q.; Wang, D. Facile fabrication of nanostructured cerium-manganese binary oxide for enhanced arsenite removal from water. *Chem. Eng. J.* **2018**, *334*, 1518–1526. [CrossRef]
48. Zeng, J.; Qi, P.; Shi, J.; Pichler, T.; Wang, F.; Wang, Y.; Sui, K. Chitosan functionalized iron nanosheet for enhanced removal of As(III) and Sb(III): Synergistic effect and mechanism. *Chem. Eng. J.* **2020**, *382*, 122999. [CrossRef]
49. You, D.; Min, X.; Liu, L.; Ren, Z.; Xiao, X.; Pavlostathis, S.G.; Luo, J.; Luo, X. New insight on the adsorption capacity of metallogels for antimonite and antimonate removal: From experimental to theoretical study. *J. Hazard. Mater.* **2018**, *346*, 218–225. [CrossRef]
50. Yan, L.; Song, J.; Chan, T.; Jing, C. Insights into antimony adsorption on {001} TiO_2: XAFS and DFT study. *Environ. Sci. Technol.* **2017**, *S1*, 6335–6341. [CrossRef]
51. Guo, X.; Wu, Z.; He, M.; Meng, X.; Jin, X.; Qiu, N.; Zhang, J. Adsorption of antimony onto iron oxyhydroxides: Adsorption behavior and surface structure. *J. Hazard. Mater.* **2014**, *276*, 339–345. [CrossRef] [PubMed]
52. Li, J.; Li, X.; Hayat, T.; Alsaedi, A.; Chen, C. Screening of Zirconium-Based Metal–Organic Frameworks for Efficient Simultaneous Removal of Antimonite (Sb(III)) and Antimonate (Sb(V)) from Aqueous Solution. *ACS Sustain. Chem. Eng.* **2017**, *5*, 11496–11503. [CrossRef]
53. Zhao, T.; Tang, Z.; Zhao, X.; Zhang, H.; Wang, J.; Wu, F.; Giesy, J.P.; Shi, J. Efficient removal of both antimonite (Sb(iii)) and antimonate (Sb(v)) from environmental water using titanate nanotubes and nanoparticles. *Environ. Sci. Nano* **2019**, *6*, 834–850. [CrossRef]
54. Iqbal, M.; Saeed, A.; Edyvean, R.G. Bioremoval of antimony(III) from contaminated water using several plant wastes: Optimization of batch and dynamic flow conditions for sorption by green bean husk (*Vigna radiata*). *Chem. Eng. J.* **2013**, *225*, 192–201. [CrossRef]
55. Pena, M.; Meng, X.; Korfiatis, G.P.; Jing, C. Adsorption Mechanism of Arsenic on Nanocrystalline Titanium Dioxide. *Environ. Sci. Technol.* **2006**, *40*, 1257–1262. [CrossRef]
56. Han, L.; Sun, H.; Ro, K.S.; Sun, K.; Libra, J.A.; Xing, B. Removal of antimony (III) and cadmium (II) from aqueous solution using animal manure-derived hydrochars and pyrochars. *Bioresour. Technol.* **2017**, *234*, 77–85. [CrossRef]
57. Buschnann, J.; Sigg, L. Antimony(III) Binding to Humic Substances: Influence of pH and Type of Humic Acid. *Environ. Sci. Technol.* **2004**, *38*, 4535–4541. [CrossRef] [PubMed]
58. Liu, C.; Li, Y.; Wang, X.; Li, B.; Zhou, Y.; Liu, D.; Liu, D.; Liu, S. Efficient extraction of antimony(III) by titanate nanosheets: Study on adsorption behavior and mechanism. *Ecotoxicol. Environ. Saf.* **2021**, *207*, 111271. [CrossRef] [PubMed]
59. Thammawong, C.; Opaprakasit, P.; Tangboriboonrat, P.; Sreearunothai, P. Prussian blue-coated magnetic nanoparticles for removal of cesium from contaminated environment. *J. Nanopart. Res.* **2013**, *15*, 1–10. [CrossRef]
60. Liu, Y.; Wu, P.; Liu, F.; Li, F.; An, X.; Liu, J.; Wang, Z.; Shen, C.; Sand, W. Electroactive Modified Carbon Nanotube Filter for Simultaneous Detoxification and Sequestration of Sb(III). *Environ. Sci. Technol.* **2019**, *53*, 1527–1535. [CrossRef]
61. Zhao, X.; Dou, X.; Mohan, D.; Pittman, C.U.; Ok, Y.S.; Jin, X. Antimonate and antimonite adsorption by a polyvinyl alcohol-stabilized granular adsorbent containing nanoscale zero-valent iron. *Chem. Eng. J.* **2014**, *247*, 250–257. [CrossRef]
62. Mishra, S.; Dwivedi, J.; Kumar, A.; Sankararamakrishnan, N. Removal of antimonite (Sb(iii)) and antimonate (Sb(v)) using zerovalent iron decorated functionalized carbon nanotubes. *RSC Adv.* **2016**, *6*, 95865–95878. [CrossRef]
63. Liu, Y.; Liu, F.; Qi, Z.; Shen, C.; Li, F.; Ma, C.; Huang, M.; Wang, Z.; Li, J. Simultaneous oxidation and sorption of highly toxic Sb(III) using a dual-functional electroactive filter. *Environ. Pollut.* **2019**, *251*, 72–80. [CrossRef] [PubMed]
64. De Miguel, E.; Izquierdo, M.; Gómez, A.; Mingot, J.; Barrio-Parra, F. Risk assessment from exposure to arsenic, antimony, and selenium in urban gardens (Madrid, Spain). *Environ. Toxicol. Chem.* **2017**, *36*, 544–550. [CrossRef] [PubMed]
65. Wang, N.; Wang, N.; Tan, L.; Zhang, R.; Zhao, Q.; Wang, H. Removal of aqueous As(III) Sb(III) by potassium ferrate (K_2FeO_4): The function of oxidation and flocculation. *Sci. Total Environ.* **2020**, *726*, 138541. [CrossRef] [PubMed]
66. Saleh, T.A.; Sarı, A.; Tuzen, M. Effective adsorption of antimony(III) from aqueous solutions by polyamide-graphene composite as a novel adsorbent. *Chem. Eng. J.* **2017**, *307*, 230–238. [CrossRef]
67. Lan, B.; Wang, Y.; Wang, X.; Zhou, X.; Kang, Y.; Li, L. Aqueous arsenic (As) and antimony (Sb) removal by potassium ferrate. *Chem. Eng. J.* **2016**, *292*, 389–397. [CrossRef]
68. Tu, Y.; Ren, L.-F.; Lin, Y.; Shao, J.; He, Y.; Gao, X.; Shen, Z. Adsorption of antimonite and antimonate from aqueous solution using modified polyacrylonitrile with an ultrahigh percentage of amidoxime groups. *J. Hazard. Mater.* **2020**, *388*, 121997. [CrossRef]
69. He, X.; Min, X.; Luo, X. Efficient Removal of Antimony (III, V) from Contaminated Water by Amino Modification of a Zirconium Metal–Organic Framework with Mechanism Study. *J. Chem. Eng. Data* **2017**, *62*, 1519–1529. [CrossRef]
70. Zhou, Z.; Dai, C.; Zhou, X.; Zhao, J.; Zhang, Y. The Removal of Antimony by Novel NZVI-Zeolite: The Role of Iron Transformation. *Water Air Soil Pollut.* **2015**, *226*, 76. [CrossRef]
71. Sun, Q.; Liu, C.; Alves, M.E.; Ata-Ul-Karim, S.T.; Zhou, D.M.; He, J.Z.; Cui, P.X.; Wang, Y.J. The oxidation and sorption mechanism of Sb on δ-MnO_2. *Chem. Eng. J.* **2018**, *342*, 429–437. [CrossRef]

72. Jia, X.; Zhou, J.; Liu, J.; Liu, P.; Yu, L.; Wen, B.; Feng, Y. The antimony sorption and transport mechanisms in removal experiment by Mn-coated biochar. *Sci. Total Environ.* **2020**, *724*, 138158. [CrossRef]
73. Zhang, W.; Zhang, G.; Liu, C.; Li, J.; Zheng, T.; Ma, J.; Wang, L.; Jiang, J.; Zhai, X. Enhanced removal of arsenite and arsenate by a multifunctional Fe-Ti-Mn composite oxide: Photooxidation, oxidation and adsorption. *Water Res.* **2018**, *147*, 264–275. [CrossRef] [PubMed]
74. Du, Y.; Qiu, S.; Zhang, X.; Nie, G. Nanoconfined hydrous titanium oxides with excellent acid stability for selective and efficient removal of As(V) from acidic wastewater. *Chem. Eng. J.* **2020**, *400*, 125907. [CrossRef]
75. Ge, X.; Liu, J.; Song, X.; Wang, G.; Zhang, H.; Zhang, Y.; Zhao, H. Hierarchical iron containing γ-MnO2 hollow microspheres: A facile one-step synthesis and effective removal of As(III) via oxidation and adsorption. *Chem. Eng. J.* **2016**, *301*, 139–148. [CrossRef]
76. Wang, H.; Wang, Y.N.; Sun, Y.; Pan, X.; Zhang, D.; Tsang, Y.F. Differences in Sb(V) and As(V) adsorption onto a poorly crystalline phyllomanganate (δ-MnO2): Adsorption kinetics, isotherms, and mechanisms. *Process Saf. Environ. Prot.* **2018**, *113*, 40–47. [CrossRef]
77. Herranz, T.; Rojas, S.; Ojeda, M.; Pérez-Alonso, F.J.; Terreros, P.; Pirota, K.; Fierro, J.L.G. Synthesis, Structural Features, and Reactivity of Fe-Mn Mixed Oxides Prepared by Mi-croemulsion. *Chem. Mater.* **2006**, *18*, 2364–2375. [CrossRef]
78. Biesinger, M.C.; Payne, B.P.; Grosvenor, A.P.; Lau, L.W.; Gerson, A.R.; Smart, R.S.C. Resolving surface chemical states in XPS analysis of first row transition met-als, oxides and hydroxides: Cr, Mn, Fe, Co and Ni. *Appl. Surf. Sci.* **2011**, *257*, 2717–2730. [CrossRef]
79. Esfandiari, N.; Kashefi, M.; Mirjalili, M.; Afsharnezhad, S. Role of silica mid-layer in thermal and chemical stability of hierarchical Fe3O4-SiO2-TiO2 nanoparticles for improvement of lead adsorption: Kinetics, thermodynamic and deep XPS investigation. *Mater. Sci. Eng. B* **2020**, *262*, 114690. [CrossRef]
80. Guo, S.; Wang, S.; Wu, N.; Liu, J.; Ni, Y.; Liu, W. Facile synthesis of porous Fe_2TiO_5 microparticulates serving as anode material with enhanced electrochemical performances. *RSC Adv.* **2015**, *5*, 103767–103775. [CrossRef]
81. Liu, G.; Debnath, S.; Paul, K.W.; Han, W.; Hausner, D.B.; Hosein, H.A.; Michel, F.M.; Parise, J.B.; Sparks, D.L.; Strongin, D.R. Characterization and Surface Reactivity of Ferrihydrite Nanoparticles Assembled in Ferri-tin. *Langmuir* **2006**, *22*, 9313–9321. [CrossRef] [PubMed]
82. Yang, F.; Zhang, S.; Cho, D.W.; Du, Q.; Song, J.; Tsang, D.C. Porous biochar composite assembled with ternary needle-like iron-manganese-sulphur hy-brids for high-efficiency lead removal. *Bioresour. Technol.* **2019**, *272*, 415–420. [CrossRef] [PubMed]
83. Yang, J.; Zhao, Y.; Ma, S.; Zhu, B.; Zhang, J.; Zheng, C. Mercury Removal by Magnetic Biochar Derived from Simultaneous Activation and Magnetiza-tion of Sawdust. *Environ. Sci. Technol.* **2016**, *50*, 12040–12047. [CrossRef] [PubMed]
84. Decarlo, E.H.; Zeltlln, H.; Fernando, Q. Simultaneous Separation of Trace Levels of Germanium, Antimony, Arsenic, and Sele-nium from an Acid Matrix by Adsorbing Colloid Flotation. *Anal. Chem.* **1981**, *53*, 1104–11077. [CrossRef]